Freezing, melting and structure of ice in a hydrophilic nanopore

Emily B. Moore,[a] Ezequiel de la Llave,[b] Kai Welke,[a] Damian A. Scherlis[b] and Valeria Molinero*[a]

Received 22nd September 2009, Accepted 28th January 2010
First published as an Advance Article on the web 26th February 2010
DOI: 10.1039/b919724a

The nucleation, growth, structure and melting of ice in 3 nm diameter hydrophilic nanopores are studied through molecular dynamics simulations with the mW water model. The melting temperature of water in the pore was T_m^{pore} = 223 K, 51 K lower than the melting point of bulk water in the model and in excellent agreement with experimental determinations for 3 nm silica pores. Liquid and ice coexist in equilibrium at the melting point and down to temperatures as low as 180 K. Liquid water is located at the interface of the pore wall, increasing from one monolayer at the freezing temperature, T_f^{pore} = 195 K, to two monolayers a few degrees below T_m^{pore}. Crystallization of ice in the pore occurs through homogeneous nucleation. At the freezing temperature, the critical nucleus contains ~75 to 100 molecules, with a radius of gyration similar to the radius of the pore. The critical nuclei contain features of both cubic and hexagonal ice, although stacking of hexagonal and cubic layers is not defined until the nuclei reach ~150 molecules. The structure of the confined ice is rich in stacking faults, in agreement with the interpretation of X-ray and neutron diffraction experiments. Though the presence of cubic layers is twice as prevalent as hexagonal ones, the crystals should not be considered defective *Ic* as sequences with more than three adjacent cubic (or hexagonal) layers are extremely rare in the confined ice.

1. Introduction

Confinement is known to affect the phase behavior of liquids.[1] Water is arguably the most studied liquid in bulk and in confinement due to its relevance in technology and the natural sciences, from biology to geology. Understanding how the anomalous thermodynamics and phase diagram of water depend on the characteristic dimensions of confinement is an active research area of fundamental and practical interest.[2] MCM-41 and SBA-15 nanoporous silica are widely used in studies of water confined in cylindrical geometries, as these materials provide well defined arrays of monodisperse cylindrical nanopores with a tunable diameter from 2 to 10 nm. NMR analysis indicates that MCM-41 pores (2–4.4 nm diameter) have an atomically smooth interior surface, while SBA-15 presents a more corrugated interface.[3,4] The melting and freezing behavior of water in silica pores has been characterized through NMR, differential scanning calorimetry (DSC), and neutron and X-ray diffraction.[5–10] These studies show that the melting temperature of ice in the pores is depressed with respect to the bulk. The depression in the melting point can be represented by a modified Gibbs–Thomson equation taking into account that the effective radius of the confined ice cylinder is smaller than the radius R of the pore, due to the existence of a water layer of width d that is not crystallized at T_m,[6] $\Delta T_m = K_{GT}/(R - d)$. The Gibbs–Thomson constant, K_{GT}, can be derived from classical thermodynamics by adding an interfacial term to the free energy of each phase. Under the assumption that the liquid phase completely wets the pore, the decrease in the melting point depends only on properties of bulk water. For a cylindrical nanopore[6] $K_{GT} = 2T_m^{bulk}\gamma_{ice-liquid}V_{liquid}/\Delta H_m$, where V_{liquid} is the molar volume of the liquid phase, $\gamma_{ice-liquid}$ is the interfacial tension between ice and liquid, and ΔH_m is the enthalpy of melting of ice. The value of the constant, evaluated from the experimental bulk quantities at T_m^{bulk} is K_{GT} = 52.4 K nm.[9] From the analysis of ice melting in MCM-41 and SBA-15 silica pores with radii ranging from 2 to 12 nm, the constants were fitted to $K_{GT} = 49.5 \pm 2$ K nm and $d = 0.35 \pm 0.4$ nm,[5] $K_{GT} = 52 \pm 2$ K nm and $d = 0.38 \pm 0.06$ nm,[7] and $K_{GT} = 52.4 \pm 0.6$ K nm and $d = 0.6 \pm 0.01$ nm.[6] A recent study of the melting point depression in acid-functionalized SBA-15 silica pores (for which the walls were decorated with carboxylic, phosphonic and sulfonic acid) revealed that the change in water–pore interactions has an extremely weak effect on ΔT_m.[11] The freezing temperature T_f of water in the nanopores also decreases with the radius of the pore. Although freezing—contrary to melting—is a non-equilibrium process, a modified Gibbs–Thomson equation was also found to fit the depression in T_f.[11] More intriguing, the temperature gap between freezing and melting, as well as the enthalpy of melting, vanish for pores of a diameter ~2.7 nm.[6,11] This effect has been attributed to the end of the first-order character of the crystallization transition under conditions of extreme confinement.[6]

[a] *Department of Chemistry, University of Utah, 315 South 1400 East, Salt Lake City, UT 84112-0850, USA. E-mail: Valeria.Molinero@utah.edu*
[b] *Departamento de Química Inorgánica, Analítica y Química Física, Facultad de Ciencias Exactas y Naturales, Universidad de Buenos Aires, Ciudad Universitaria, Buenos Aires, Pab II, C1428EHA, Argentina*

The T_f, T_m and ΔH_m of water in the nanopores have been determined accurately from NMR and DSC analysis. The structure of water in the crystallized nanopores, however, remains elusive. The modified Gibbs–Thomson relation suggests the presence of a non-freezable water layer, but it provides no insight into its structure nor is it accurate in describing its width (partly because the radii of the pores are subject to uncertainties and reported values depend on the measurement techniques). NMR results show evidence of the presence of mobile components in the nanopores that have been interpreted as viscous liquid and a plastic form of ice.[12] NMR cannot indicate, however, the localization of the liquid inside the pore, *e.g.* whether all the liquid is at the interface. Neutron diffraction studies of filled and partly filled SBA-15 pores show the existence of defective cubic ice and an amorphous component in the crystallized pore.[13–15] It should be noted that cubic ice formed in bulk samples does not have a pure cubic structure but contains hexagonal stacking faults (evident in the form of the 100 peak of *Ih* in the diffraction patterns), in amounts that depend on the method and experimental conditions under which the ice is formed.[16–19] Liu *et al.* conjectured that there is an interfacial region between the ice at the center of the $R = 4.3$ nm pore and its surface that contains a disordered form of water/ice, which reversibly converts to ice at lower temperatures.[13] X-ray diffraction studies of MCM-41 and SBA-15 pores of diameter 4.4–72 nm also provide evidence of the presence of a hexagonal and cubic ice hybrid, although no features characteristic of hexagonal ice were found for pores of diameter 4.4 nm.[20] Morishige and Uematsu modeled the experimental diffraction pattern as arising from hexagonal ice with a certain probability of stacking faults; they found that the density of faults decreased as the pores become wider and proposed that the stacking sequences of the confined ice are nearly random.[20]

Molecular simulations have a spatial resolution that makes them optimum for the study of ice structure in the nanopores, the existence and distribution of a liquid phase and of the melting, nucleation and growth processes. The study of water crystallization through atomistic simulations, however, is challenging, as crystallization requires spontaneous nucleation of small crystallites and their growth. Ice nucleation is a stochastic rare event, and its modeling through simulations requires either extensive sampling involving very long simulations or the use of simulation techniques to sample rare events. The first strategy, also known as the ''brute force'' approach, was pursued in the studies of the nucleation of ice from bulk water,[21] from a system with a water–vacuum interface,[22] from water confined between planar surfaces[23–30] and in narrow carbon nanotubes.[31] Spontaneous crystallization of water in simulations of hydrophilic cylindrical nanopores has not been reported to date. The second strategy has been applied to study the nucleation of bulk ice through Monte Carlo (MC) simulations with umbrella sampling along a predefined reaction coordinate that accounts for the global change in symmetry as liquid water transforms into ice,[32,33] and through metadynamics simulations,[34] which favored the crossing of nucleation barriers along the same reaction coordinate as in ref. 32. The umbrella sampling[25] and the metadynamics[27] simulations led to different results, predicting, respectively, hexagonal (*Ih*) and cubic (*Ic*) ice to be the product of crystallization, in spite of using the same TIP4P model under equal temperature and pressure conditions, and applying biased sampling along the same reaction coordinates. *Ih* is the stable crystal of TIP4P water at room pressure.[35,36] Brukhno *et al.* introduced a maximum projection method that distinguishes cubic and hexagonal ice, which they used to bias the formation of ice in parallel tempering umbrella sampling MC simulations.[33] Their method as is cannot be used to recognize *Ih* and *Ic* arbitrarily oriented in the simulation cell (because it is not rotationally invariant), although it is adequate to grow ice with hexagonal and cubic stacking in a predetermined fixed orientation. The orientation of the stacking faults in confined ice, however, is not known beforehand and the axis of the stacking (the *c*-axis) may change directions as the crystal grows along the pore.

In this work, we use molecular dynamics simulations to address the following questions: how do the temperatures of melting and freezing of water in the nanopore compare with bulk water, how does water nucleate and grow ice in a hydrophilic nanopore, and what is the structure of the crystallized water in the pore. The most critical challenges faced by molecular simulations of nucleation and growth of ice, and the recognition of its structure, are:

(i) The accuracy of the water models. Of the most popular atomistic models of water, only TIP4P predicts that ice *Ih* is the most stable phase, while TIP3P, SPC, SPC/E and TIP5P predict that ice *II* is the stable crystal at room pressure.[37,38] The melting point of *Ih* with TIP4P is 232 K;[37] an improved version of the model, TIP4P/ice predicts 272.2 K.[39] The melting point of *Ic* for the TIP4P/ice model has not been reported to date.

(ii) The computational cost of atomistic simulations limits the studies to small systems (to date, less than 800 molecules simulated with classical methods using rigid water potentials). In the case of ''brute force'' simulations, this cost hinders the production of enough unconstrained simulations to extract information on the size of the critical nuclei and mechanisms of crystallization.

(iii) Methods to sample rare events relying on the mapping of the free energy along a reaction coordinate for the nucleation and growth seem to give either inconsistent structures or be limited to growing ice in predetermined directions, making them inadequate to elucidate the stacking structure of ice in the nanopores.

(iv) The lack of simple to implement rotationally invariant methods to identify the growth of hexagonal and cubic ice, as pure crystals or in randomly oriented stacked configurations.

In this work we address (i) and (ii) by using the mW coarse-grained model of water whose computational implementation is 180 times more efficient than that of atomistic models with Ewald sums,[40] yet accurately describes the thermodynamics and structures of liquid water, *Ih* and *Ic*. The monatomic water model mW represents each water molecule by a single particle with three-body nonbonding interactions that mimic hydrogen bonds.[40] mW reproduces the structure of water phases (ice, clathrates, liquid, low density amorphous ice),[40–42] the thermodynamic anomalies of water and the enthalpy of the phase transitions between liquid, vapor and

ice with comparable or better accuracy than the most popular atomistic water models, including TIP4P/ice.[40] Important for this study, mW predicts that the most stable crystal is hexagonal ice, with melting temperature $T_m^{Ih} = 274$ K. mW predicts that cubic ice is slightly less stable, $T_m^{Ic} = 271$ K, in excellent agreement with the 271.7 K estimated from thermodynamic cycles.[43] While the thermodynamics and structure of water are well represented by the mW model,[40–42] water mobility is not. Although mW correctly describes the well-known diffusion anomaly of water (the existence of a diffusivity maximum on compression), it does not reproduce the characteristic times of diffusion of the liquid.[40] The diffusivity of liquid mW water is about twice the experimental value at room temperature, with the difference increasing upon cooling. The diffusion coefficient of mW is less sensitive to temperature than found in experiments because the energy of the coarse-grained model only depends on the oxygen positions, and thus it does not account for the full barrier of breaking hydrogen bonds as water diffuses. We note, however, that the energy of the hydrogen bonds is well accounted for in mW, which reproduces the enthalpies of vaporization and melting within just 0.17 kcal mol^{-1} of the experimental values;[40] it is the *barrier* for breaking the bonds that is smaller, not the energy difference between stable states. The faster dynamics of mW is an asset for the study of crystallization, as both nucleation and growth rates are enhanced in the coarse-grained model. Thus, in addition to the 180 times increase in efficiency of the mW model (measured in terms of the computing time required to simulate a fixed amount of time, *e.g.* 10 ns, for a given number of molecules), the rate of nucleation and growth of ice in the mW model is enhanced due to the faster intrinsic dynamics of the coarse-grained water. This makes it possible to produce an ensemble of crystallizing trajectories through unconstrained (''brute force'') MD simulations of supercooled water, the approach we take in this work.

The last challenge, the recognition of hexagonal and cubic ice, is addressed with a novel, simple method that makes use of the correlation of bond order parameters[44,45] to compute the number of staggered and eclipsed intermolecular O$\cdots$O bonds that distinguish the two polymorphs. The method we introduce in this work is easy to implement and recognizes *Ic*, *Ih* and any hybrids of the two, irrespective of the orientation of the crystallites in space. This feature makes it particularly suitable to characterize the structure of ice as it grows in the anisotropic environment of the nanopore, without assuming that the stacking faults have a preferred alignment with the axis of the pore.

We present a study of the nucleation, growth, structure and melting of ice in a cylindrical hydrophilic nanopore with an internal diameter of 3 nm. For this work, we select a simple—idealized—pore: the pore wall itself is made of water. The configuration of the molecules of the wall corresponds to that of liquid water at 298 K. The molecules of the pore wall are allowed to vibrate, but they are restrained from diffusing away through soft harmonic intermolecular bonds with their closest neighbors in the wall. The intermolecular interactions of water with the wall are the same as for water with itself. The rationale for studying the melting and freezing of water in a water–wall pore is that under the assumption of complete wetting of the pore wall by water, the Gibbs–Thomson constant depends only on bulk water properties. The implication is that for a fully wetting surface the equilibrium melting temperature of water in the pore depends on the radius of the pore, but not on the chemical details of its surface. This corollary agrees with the results of recent experiments, in which it was found that decoration of the surface of SBA-15 silica with acid groups did not affect the melting and freezing temperatures of water.[11] Experimental studies on MCM-41 and SBS-15 silicas suggest that even in the crystallized pore there may be a layer of liquid water wetting the pore wall.[5–7,12–15] Based on these arguments, we expect that the thermodynamics of melting and freezing of water reported for water confined in SBS-15 and MCM-41 silica are common to other hydrophilic nanopores for which water wets completely the surface, such as the one selected for this study.

The paper is organized as follows: section 2 describes the simulation methods and models. Section 3 presents a new method for the identification of ice polymorphs and shows the equivalence to crystallographic methods for the classification of stacking faults in ice. Section 4 presents the results for the nanopores and section 5 the most important conclusions of this work.

2. Simulation model and methods

Water potential

The monatomic water model mW consists of a sum of pairwise, ϕ_2, and three-body, ϕ_3, contributions:[40]

$$E = \sum_i \sum_{j>i} \phi_2(r_{ij}) + \sum_i \sum_{j\neq i} \sum_{k>j} \phi_3(r_{ij}, r_{ik}, \theta_{ijk})$$

$$\phi_2(r_{ij}) = A\varepsilon\left[B\left(\frac{\sigma}{r_{ij}}\right)^{p_{ij}} - \left(\frac{\sigma}{r_{ij}}\right)^{q_{ij}}\right]\exp\left(\frac{\sigma}{r_{ij}-a\sigma}\right)$$

$$\phi_3(r_{ij}, r_{ik}, \theta_{ijk}) = \lambda\varepsilon[\cos\theta_{ijk} - \cos\theta_0]^2 \times \exp\left(\frac{\gamma\sigma}{r_{ij}-a\sigma}\right)\exp\left(\frac{\gamma\sigma}{r_{ik}-a\sigma}\right) \quad (1)$$

where r_{ij} is the distance between particles i and j, θ_{ijk} is the angle formed by the vectors $\dot{r}_{ij}$ and $\dot{r}_{ik}$, $A = 7.049556277$, $B = 0.6022245584$, $p = 4$, $q = 0$, $\gamma = 1.2$, $a = 1.8$, $\theta_0 = 109.47^\circ$, $\sigma = 2.3925$ Å, $\varepsilon = 6.189$ kcal mol^{-1}, and $\lambda = 23.15$. The three-body term adds an energy penalty to configurations with angles that depart from θ_0, encouraging ''hydrogen bonded'' tetrahedral configurations. The mW model does not have electrostatics or hydrogen atoms. The short-range of the potential (less than 4.32 Å) and the lack of hydrogen atoms, allowing for longer integration steps, makes mW 180 times faster than atomistic simulations of rigid models with Ewald sums. We refer the interested reader to ref. 40 for the details on the parameterization, validation, benchmarking and evaluation of the mW model.

Pore systems

The pore-wall and the liquid contained in the pore were made of water. An open cylindrical nanopore was built from an

instantaneous configuration of liquid water containing 12 288 coarse-grained molecules equilibrated at 298 K and 1 atm (density 0.997 g cm^{-3}) in a simulation cell 5 nm wide in the x and y directions and about 15 nm long in the z direction. The molecules in this configuration were assigned to two groups, according to their position: *pore wall* and *water*. The *pore wall* was made of the particles found (a) outside a cylinder of radius 1.5 nm from the center of the block in (x,y) and (b) their z positions were not in the first 1 nm slab of the block:

$$(x_i - x_{\text{center}})^2 + (y_i - y_{\text{center}})^2 \geq (1.5\ \text{nm})^2 \cap z_i > 1\ \text{nm} \quad (2)$$

This defines a pore wall made of 7859 particles forming an open cylindrical pore of radius 1.5 nm and length 14 nm. The remaining 4429 particles form the *water* phase. The water phase was T-shaped, with a flexible 1 nm length head block that allows for expansion of the liquid on cooling and crystallization. The nonbonding interactions between *all* particles were described with the mW model. The particles in the pore wall vibrate like in a solid: the wall molecules were restrained around their original intermolecular distances through harmonic bond potentials, $K(r_{ij} - r_{ij}^{o})^2$, with their first neighbors within the wall ($r_{ij}^{o} < 3.5$ Å). We used a soft bond constant, $K = 30$ kcal $Å^{-2}$, compatible with the large time step of the mW model (10 fs, see below) but sufficient to ensure that the intermolecular structure of the wall remains the one of the equilibrium configuration of liquid water at 298 K from which the pore wall was made. The pore wall vibrates like a solid but it has the structure (in terms of intermolecular distances and angles) of liquid water at 298 K. From the point of view of the water inside the pore, the wall presents the structure and interactions of liquid water. To quantify the roughness of the pore wall, we computed the width over which the radial density of the wall, measured from the center of the pore, decays from 90 to 10% of its bulk matrix value. The $t_{10\text{–}90}$ computed over a 100 ns trajectory of the pore filled with water at 200 K was 1.45 Å.

Simulation methods

We carried out molecular dynamics simulations in the *NPT* ensemble using LAMMPS.[46] The equations of motion were integrated with the Velocity Verlet algorithm with a time step of 10 fs. The systems were simulated with periodic boundary conditions. The temperature was controlled with a Nose–Hoover thermostat with relaxation time 0.5 ps. The pressure was controlled at $p = 1$ atm through a Nose–Hoover barostat with time constant 2.5 ps. The z dimension of the cell was allowed to dilate and contract independently of the x and y dimensions, to account for the anisotropy introduced by the pore.

Tetrahedral order and alignment in bulk reference systems

Periodic cells of *Ih* and *Ic*, containing 576 and 512 water particles, respectively, were built using crystallographic data. The simulation cells for low-density amorphous ice (LDA, the glass of water) and liquid water contained 512 water molecules each, simulated at 150 and 298 K, respectively. The LDA was produced by cooling of the bulk liquid at the critical vitrification rate, following the protocols of ref. 41. The tetrahedral order parameter q_t and orientational alignment a (eqn (3) and (5), see section 3) were computed from 200 configurations extracted from 0.5 ns simulations.

Freezing temperature

To compute the fastest cooling rate that produces ice crystallization and the freezing temperature T_f^{pore}, liquid water in the pore was first equilibrated at 220 K for 20 ns and subsequently cooled from 220 to 180 K at linear rates 10, 1, 0.5, 0.2 and 0.1 K ns^{-1}. Each temperature ramp was simulated by setting the target temperature of the thermostat as a linear function of time. Crystallization was quantified through the analysis of the total number of molecules in the ice phase, N_{ice}, and the number of molecules in the largest ice nuclei, $N_{\text{largest ice cluster}}$, as a function of temperature. T_f^{pore} was considered to be that for the onset of ice growth in the system.

Isothermal freezing of water in the nanopore

To garner statistics on the process of crystallization and the structure of ice in the nanopore, we performed ten independent simulations at T_f^{pore}. These simulations started from uncorrelated configurations from a simulation of liquid water in the pore at 220 K, quenched instantaneously to T_f^{pore} and evolved for 80 to 170 ns, until the crystallization of water in the pore was complete. Completion of the crystallization was monitored through the time evolution of the energy and the number of molecules in the ice phase.

Melting temperature of ice in the nanopore

We determined the melting temperature T_m^{pore} for ice in the pore from constant temperature simulation of fully crystallized systems (the result of the crystallization simulations described above) at $p = 1$ atm and $T = 220$, 225, 230 and 235 K for 10 ns. The enthalpy of melting was computed from the difference of the enthalpy of water in the pore at the lowest temperature for which all water in the pore is liquid and the highest temperature for which there is ice in the pore, divided by the total number of molecules in the water phase.

3. Identification of ice

Here we introduce a simple method to identify hexagonal and cubic ice as crystallization proceeds from liquid water. Two challenges must be addressed: the first is to distinguish liquid from crystal, and the second is to differentiate *Ic* and *Ih* polymorphs.

The *CHILL* algorithm

To distinguish liquid from crystal we adopt the local bond order parameter method developed by ten Wolde *et al.* for the identification of crystal nuclei in Lennard-Jones systems,[45] based on the order parameters introduced by Steinhardt *et al.*[44] In this method, molecules are classified as belonging to the crystal or liquid based on the coherence of their orientational order with that of their neighbors. The analysis of the coherence of local ordering rather than the local ordering itself is particularly critical for the identification of ice from deeply supercooled liquid water, as the structure of the latter becomes increasingly tetrahedral on cooling,

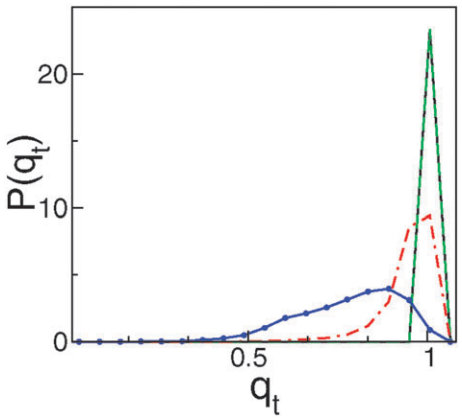

Fig. 1 Probability density of the tetrahedral order parameter q_t shown for *Ih* (solid black), *Ic* (dashed green), low-density amorphous ice LDA (dash-dotted red) and room temperature liquid water (dotted blue). Note that the distributions for *Ih* and *Ic* overlap completely, because they both have perfectly tetrahedral environments. The overlap in $P(q_t)$ for *Ih*, *Ic* and LDA does not allow these structures to be distinguished using q_t.

acquiring the structure of a random tetrahedral network in the glass state.[41] The local tetrahedral order q_t around each molecule k is defined by[47]

$$q_t(k) = 1 - \frac{3}{8}\sum_{i=1}^{3}\sum_{j=i+1}^{4}\left(\cos\theta_{ikj} + \frac{1}{3}\right)^2 \qquad (3)$$

where θ_{ikj} is the angle subtended between the central water molecule k and two of its 4-closest neighbors. $q_t(k)$ is 1 for a tetrahedral configuration. Fig. 1 displays the distribution of local tetrahedral ordering around the water molecules in *Ih*, *Ic* and low-density amorphous ice (LDA) at 150 K, and liquid water at room temperature. $P(q_t)$ cannot distinguish the ice phases from the LDA glass. Patches of tetrahedrally coordinated molecules with LDA-like structure develop and increase in size as liquid water is cooled, rendering the distribution of tetrahedral order of the liquid increasingly overlapped with that of the crystals.[41]

The increasing tetrahedrality of liquid water on cooling hinders the possibility of using a measure of local tetrahedrality around each water molecule as classification of belonging to ice or liquid.[41] The tetrahedra centered on neighbor molecules, however, are aligned in a well-defined way in ice and randomly aligned in the liquid and glass. This difference is the basis of the identification of crystal particles of the bond order parameter method that we adopt in this work. The local order around each water i is defined by a local orientational bond order parameter vector $\dot{q}_l(i)$ with $2l + 1$ complex components

$$q_{lm}(i) = \frac{1}{4}\sum_{j=1}^{4} Y_{l,m}(\hat{r}_{ij}). \qquad (4)$$

The $q_{lm}(i)$ project the orientational structure of the four closest neighbors of a molecule on a basis of spherical harmonics $Y_{l,m}(\theta_{ij},\phi_{ij}) = Y_{l,m}(\hat{r}_{ij})$, where $\hat{r}_{ij}$ is the unit vector that connects i with one of its four closest neighbors j. The alignment of the orientation of the local structures is measured by the normalized dot product of $\dot{q}_l$ between each pair of neighbor molecules,

$$a(i,j) = \frac{\hat{q}_l(i)\cdot\hat{q}_l(j)}{|\hat{q}_l(i)||\hat{q}_l(j)|} = \frac{\sum_{m=-l}^{l} q_{lm}(i)q^*_{lm}(j)}{\left(\sum_{m=-l}^{l} q_{lm}(i)q^*_{lm}(j)\right)^{1/2}\left(\sum_{m=-l}^{l} q_{lm}(j)q^*_{lm}(i)\right)^{1/2}}, \qquad (5)$$

where q^*_{lm} is the complex conjugate of q_{lm}. To determine the optimum l that distinguishes between structures *Ih*, *Ic* and the liquid, we computed the distribution of alignments, $P_l(a)$, for $l = 1, 2, \ldots 10$ for *Ih*, *Ic* and LDA at $T = 150$ K, and liquid water at 300 K. We found that $l = 3$ and 4 provide the best resolution of these structures. In what follows we adopt $l = 3$, as it involves the least number of calculations. It should be noted that while the global orientational order parameter Q_l of the crystals is zero for $l = 3$, it is not for $l = 4$,[44] thus, classification based on the latter should be used in cases where the total order needs to be biased (*e.g.* in an umbrella sampling or metadynamics calculation) towards the formation of the crystal phase. The global order is always zero for the amorphous systems.

Fig. 2 shows the distributions of alignment between local structures for $l = 3$. Contrary to the local tetrahedrality q_t, the alignment a presents sharply distinct distributions for ice and LDA glass. Moreover, the distribution of tetrahedral alignments allows for a distinction between cubic and hexagonal ice. All water molecules in *Ih* and *Ic* are tetrahedrally coordinated. The main difference between these polymorphs is that in cubic ice all water molecules have a staggered arrangement of intermolecular bonds with respect to its four neighbors, while in hexagonal ice three of the intermolecular bonds are staggered and one, parallel to the *Ih* c-axis, is eclipsed. With

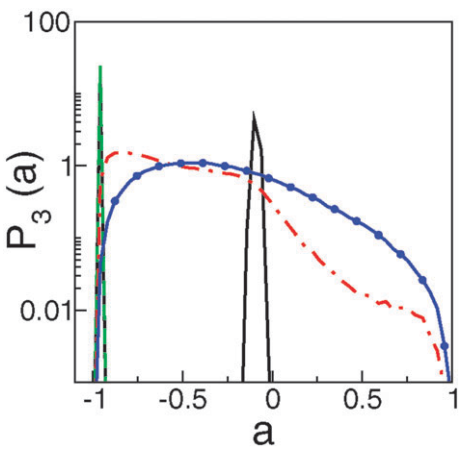

Fig. 2 Probability density of the alignment of orientational order, $P_3(a)$. Same symbols as in Fig. 1. The distribution of alignments is sharp for *Ih* and *Ic*, with a peak around $a = -1$ for both *Ih* and *Ic* that signal a staggered arrangement of intermolecular bonds (with all four neighbors in *Ic*, with three of the four neighbors in *Ih*), and a peak around $a = -0.11$ for *Ih* that corresponds to the neighbor with eclipsed configuration. We use the number of staggered and eclipsed neighbors to distinguish between molecules that belong to different ice polymorphs and the liquid.

$l = 3$, perfect staggered water–water bonds yield $a = -1$ and perfect eclipsed bonds $a = -0.11$. This provides the basis for the classification of the structures of ice and liquid as the crystallization of water proceeds in the nanopore.

We classify the molecules according to the alignment of their orientation with respect to that of its four closest neighbors into four groups:

• ***C***: A molecule that belongs to the cubic ice phase has all bonds with its four closest neighbors staggered. To allow for thermal fluctuations, we define a staggered bond as one with $a < -0.8$.

• ***H***: A molecule that belongs to the hexagonal ice phase. It has three staggered bonds ($a < -0.8$) and one eclipsed bond ($-0.2 < a < -0.05$) with its four closest neighbors.

• ***I***: A molecule that belongs to the ice phase but does not satisfy the strict requisites for being ***H*** or ***C***. This is the case for molecules in the surface of crystallites. We define ***I*** as those having (i) only two staggered bonds and at least one neighbor with more than two staggered bonds, or (ii) three staggered bonds, no eclipsed bond, and at least one neighbor with two staggered bonds. The latter allows for the identification of ice in non-compact crystallites.

• ***L***: A molecule that belongs to the liquid or amorphous phase. These are molecules that do not satisfy the requisites indicated above. ***L*** indicates that the structure is amorphous as in the liquid. The mobility of the ***L*** molecules is used to distinguish whether they form a liquid or a glass (*e.g.* LDA).

Using this algorithm, that we name *CHILL*, we find that 100% of the molecules in *Ih* are classified as *H*, 100% of the molecules in *Ic* as *C*, 0.1% of the molecules in room temperature water are classified as crystalline, and 12% of the LDA glass is classified as crystal, of which 91% is *I*. The largest ice cluster in LDA was found to contain 19 ± 8 water molecules. The finding of small ice nuclei in LDA is a consequence of the metastable nature of this phase, and not an artifact of the identification method.

Identification of stacking sequences in ice

Our classification of the ice polymorphs with the *CHILL* algorithm is based on the identification of the number of staggered and eclipsed bonds for each water molecule. The usual classification of hexagonal and cubic crystal is based on the repetition of sequences of layers: ABABAB... for hexagonal and ABDABDABD... for cubic. A fault is a break in the ordering of the sequences of the cubic or hexagonal crystal.[18] A growth fault is the incorporation of a single hexagonal (cubic) sequence in a cubic (hexagonal) lattice. An example of a cubic sequence with a growth fault is ABDA**B**A̲DBADB, where the introduction of A̲ layer, leaves **B** flanked by two identical layers, producing a hexagonal layer (*h* layer).[18] A deformation fault incorporates two adjacent hexagonal (cubic) layers in a cubic (hexagonal) sequence. An example of a deformation fault in a cubic sequence is ABDA**B**A̲B̲DABD that arises from the addition of A̲B̲ to a cubic sequence and yields two layers (**BA**) with hexagonal order. Instead of using the letters A, B and D to indicate the absolute position of the layers, it is more convenient to indicate whether the layers are hexagonal (flanked by identical ones), or cubic (flanked by distinct ones). We use lowercase *h* and *c* to denote a hexagonal and cubic layer, respectively.[17,18] In terms of our classification of the *molecules* based on the number of staggered and eclipsed bonds with their four closest neighbors, an *h* layer corresponds to the plane between two adjacent layers of *H* molecules; and a *c* layer to the plane between two layers of *C* molecules. Note that an isolated layer of *H* (or *C*) molecules is not possible, as the definition of staggered or eclipsed bonds involves always a pair. Fig. 3 illustrates the correspondence of the layer-based and molecule-based assignments for the repeated *hhc* sequence, also known as 9R.[48]

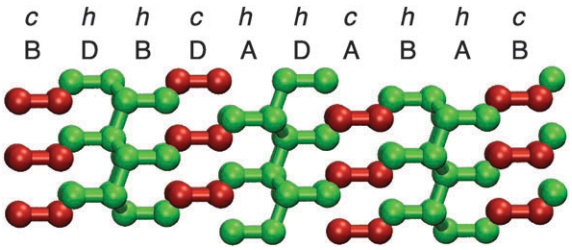

Fig. 3 Assignment of hexagonal and cubic layers for the 9R structure, a repetition of the *hhc* stacking sequence. The water molecules (hydrogen not shown) are colored according to the classification as hexagonal *H* (green) or cubic *C* (red). The lower row of labels indicate the absolute positions of the layers (here named A, B and D), and the upper label indicates whether it is a hexagonal layer *h*, or a cubic layer *c*. An easy way to visualize a *h* (or *c*) layer is to look for the plane between pairs of adjacent *H* (or *C*) molecules along the *c*-axis of the stacked crystal.

4. Results and discussion

A Freezing temperature of water in the nanopore

Although water is not a good glass former, micron-sized droplets of water can be vitrified when cooled at rates of about 10^6 K s^{-1}.[49] Due to the lack of hydrogen atoms, crystal nucleation and growth are faster in the mW model than in real water.[40] The maximum cooling rate that produces crystallization of bulk mW is $q_x = 2$ K ns^{-1} for a system of 32 768 molecules and $q_x = 1$ K ns^{-1} for 512 molecules.[40,41] The temperature of crystallization of water at q_x is $T_f^{bulk} \approx 200$ K for these systems. This temperature is about 30 K lower than for bulk experimental water, for which the temperature of homogeneous nucleation is 231 K.[50]

We quantified the degree of crystallization of water in the pore for quenching rates ranging from 10 to 0.1 K ns^{-1}. Fig. 4 shows the number of particles in the largest ice nucleus (including cubic, hexagonal and interfacial ice) along these quenching trajectories. The fastest cooling rate that leads to crystallization—albeit converting only 25% of the water into ice—is 1 K ns^{-1}. This is comparable to q_x for the bulk system, although in the bulk simulations essentially all the water was crystallized at 1 K ns^{-1}. We found that not even the slowest quenching rates lead to crystallization of all the water at 180 K. The maximum conversion to ice was 66%. The other 34% of water consists of a liquid layer of water that wets the surface of the pore (more details in 4.C and 4.D). Our results

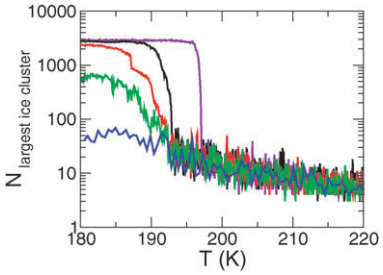

Fig. 4 Number of particles in the largest ice nucleus *versus* temperature, along the quenching trajectories with constant cooling rate 0.1 K ns^{-1} (violet), 0.2 K ns^{-1} (black), 0.5 K ns^{-1} (red), 1 K ns^{-1} (green) and 10 K ns^{-1} (blue). Crystallization is observed for $q_x \leq 1$ K ns^{-1}. The onset temperature of crystallization ranges from 196 K for the slowest ramp to 193 K for 1 K ns^{-1}. At the end of the cooling ramp, the percentage of ice was 25% of the total water in the pore for 1 K ns^{-1}, 54% for 0.5 K ns^{-1}, 62% for 0.2 K ns^{-1} and 66% for 0.1 K ns^{-1}.

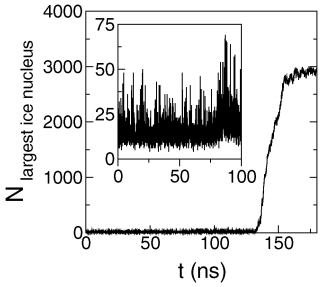

Fig. 5 Number of particles in the largest ice nucleus *versus* time for a representative crystallizing trajectory. A latent period, $0 < t < t_n = 130$ ns, is followed by ice growth. The inset shows a detail of the largest nucleus size during the latent period. From the largest size attained before nucleation, we estimate the critical nucleus size to contain about 75–100 water molecules at 195 K.

confirm the existence of mobile liquid water in the crystallized pores previously deduced from NMR and DSC measurements.

The freezing temperature of water in the pore, T_f^{pore}, ranged from 197 to 193 K for rates 0.1 K ns^{-1} to 1 K ns^{-1} (Fig. 4). The crystallization of ice in the quenching simulations started in the head of the pore for the 0.1 K ns^{-1} simulation, inside the volume confined by the pore for the 0.2 and 0.5 K ns^{-1} ones, and from different nucleation sites, inside the pore and in the head, for the 1 K ns^{-1}. We selected $T_f^{pore} = 195$ K for the studies of isothermal freezing described in the next section. The freezing point depression, measured with respect to bulk mW water is $\Delta T_f \approx 7$ K. The experimental freezing temperature of water in the 3 nm diameter pores of MCM-41 is ~213–223 K,[6,7] this is 8–18 K lower than the temperature of homogeneous nucleation of water, T_H. In separate work,[51] we show that the freezing temperature of water tracks closely the temperature of the high- to low-density transformation in the supercooled liquid.[41]

B Nucleation and growth of ice in the nanopore

Crystallization involves the nucleation and growth of ice crystallites. Fig. 5 shows the number of molecules in the largest ice nucleus as a function of time for a representative freezing trajectory at $T_f^{pore} = 195$ K. There are two well defined time regimes: an induction period during which ice nuclei containing less than 70 water particles form and dissolve, and a growth period in which the nuclei develop into larger crystals. The induction time is stochastic, for this set of ten simulations it was found to last between 52 and 134 ns. After the growth started at the nucleation time t_n, all samples crystallized within 17 ± 4 ns. From the size of the unsuccessful nuclei formed during the induction period in the isothermal and quenching trajectories, we estimate that the critical ice nucleus contains about 75–100 water molecules. The radius of gyration of the ice nuclei of critical size, 0.8–1.2 nm, is similar to the radius of the pore, 1.5 nm. The nucleation of ice is homogeneous: the formation of the nuclei is not assisted by the pore wall surface.

In all the isothermal simulations, the full pore crystallized from a single nucleus that grows to form a crystal that spans the entire pore. This is not surprising, as formation of the critical nucleus is a rare event and the volume of water in the pore is small (~100 nm^3). We found that in 8 out of 10 simulations the successful nuclei originated in the head of the pore, the ~1 nm slab at the extreme of the periodic system. It should be noted that in our simulations, the volume ratio between the water contained in the pore and its head is approximately 3 : 1. When the relative frequency of successful nucleation events is weighted by such a ratio, it turns out that the specific probability (per unit of volume) of an event leading to crystallization inside the pore is only 6% at 195 K. This result is reflecting that the growth of ice is hindered under confinement because the radius of the pore is comparable to the critical nucleation size. In experiments where the pores are usually much longer than in the simulations, we expect a larger fraction of successful nucleation events inside the pore.

Fig. 6 shows snapshots of the growth of ice in the pore. Only the water molecules that belong to the cubic (*C*) or hexagonal (*H*) polymorphs are shown. These are surrounded by interfacial ice (*I*) and embedded in the liquid (*L*). The crystallization starts with the formation of a small nucleus in which cubic and hexagonal features are present, although stacking of *h* and *c* layers are not yet evident until the nuclei reach ~150 molecules. These grow into a single crystallite comprised of well-defined stacking planes. The orientation of the stacking with respect to the axis of the pore is random, and is determined by the initial growth of the critical nucleus.

C Structure of ice in the nanopores

Fig. 7 shows representative snapshots of the confined ice after crystallization is complete. All the samples present profuse stacking of *h* and *c* layers in a continuous crystallite, with a *c*-axis that changes direction every 5.5 ± 2 nm. Table 1 summarizes the average percentages of liquid and ice (cubic, hexagonal and interfacial) in the crystallized nanopores. We verified that the molecules classified as part of the liquid phase are mobile within the time scale of the simulations. As observed in the quenching simulations, not all the water in the pore can be crystallized at $T_f^{pore} = 195$ K, although this temperature is ~30 K below the corresponding melting point (see 4.D below). Liquid water accounts for 37.4 ± 4.4% of the equilibrium contents of the pore at 195 K. Most of the liquid, 88 ± 6%, is in the first monolayer that wets the pore

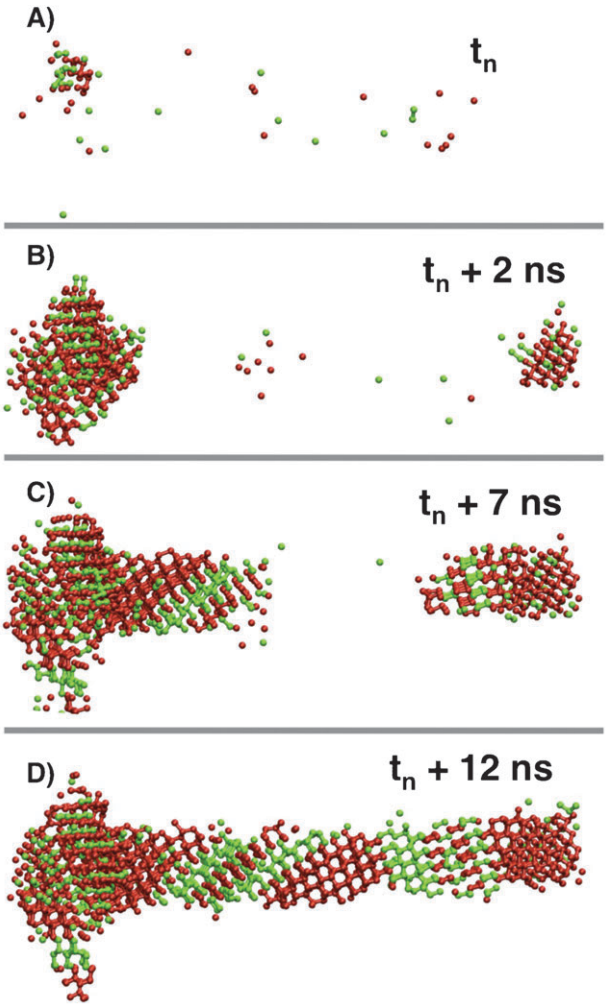

Fig. 6 Progression of crystallization from the nucleation time, t_n, for a representative crystallizing trajectory. Only the hexagonal *H* (green) and cubic *C* (red) water particles are shown. The largest ice nucleus (including hexagonal, cubic and interfacial ice) along this progression contains 127, 1021, 2109 and 2844 molecules. Note that the system crystallizes from a single ice nucleus, which appears to grow from the left and right side of the figure due to the periodic boundary conditions of the simulations. The stacking directions are not well defined for the critical nucleus, but develop soon afterwards and are already well defined 2 ns after nucleation.

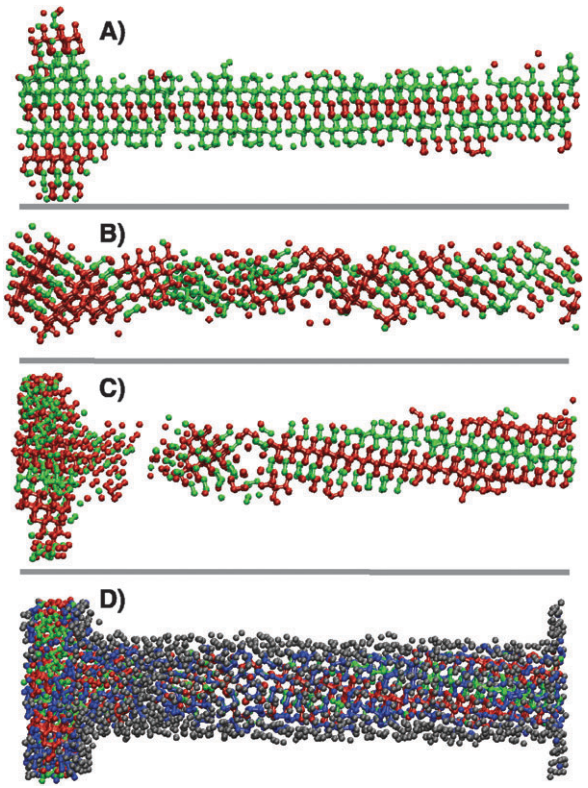

Fig. 7 Configurations of the confined ice at the freezing temperature. Panels A, B and C show the cubic (red) and hexagonal (green) components of the ice formed in three different simulations. The lower panel displays also the interfacial ice (blue) and liquid (grey) of the configuration of panel C.

wall. Of this wetting layer, $\frac{3}{4}$ of its molecules are liquid and the other $\frac{1}{4}$ belong to interfacial ice (Table 1).

The ratio of cubic to hexagonal ice in the pore is about 2 : 1 (Table 1). The energy of bulk *Ih* and *Ic* are similiar: at 195 K the mW model predicts $H_{Ic} - H_{Ih} = 0 \pm 30$ J mol^{-1}, in good agreement with the 35 J mol^{-1} measured with adiabatic calorimetry.[52] In spite of the variety of stacking arrangements found in the ten crystallized pores, their energies per mole of water were identical within 80 J. This suggests that stacking does not affect significantly the energy of the crystals, and is consistent with the almost random arrangement of *h* and *c* layers observed in these pores. From the analysis of the stacking sequences of the ten pores, we computed the probabilities for pairs of layers of type *hh*, *hc*, *ch* and *cc* to be followed by a *c* layer.[17,19] These are, respectively, $\alpha = 0.72$, $\beta = 0.71$, $\gamma = 0.70$ and $\delta = 0.61$. Note that the probability that two hexagonal layers are followed by a third *h*, $1 - \alpha = 0.28$, is much lower than the probability of *c* following a *cc* sequence, $\delta = 0.61$. Hansen *et al.* obtained the same qualitative result from their analysis of the diffraction patterns of bulk ice I formed by decompression of ice V and IX.[17] Morishige and Uematsu estimated the growth fault probability α from the analysis of the diffraction patterns of ice in silica nanopores: they reported values of α which increase from 0.1 to 0.53 as the pore diameter narrows from 72 to 9.8 nm.[20] The value we find for the 3 nm pore, $\alpha = 0.72$, is consistent with an extrapolation of the trend towards higher growth fault probability deduced from their X-ray diffraction experiments.

The diffraction patterns on ref. 17 indicate that the hexagonal sequences in ice I obtained from decompression of ice V and IX appear mainly in pairs (deformation faults) and rarely as singles (growth faults). This is not the case in the narrow $R = 1.5$ nm nanopores: we find four times as many hexagonal growth faults (a *chc* sequence) than hexagonal deformation faults (*chhc* sequence). The ratio is almost 1 : 1 for the cubic faults (*hch vs. hcch* sequences). Cubic and hexagonal deformation faults (*hcch vs. chhc*) occur in a 3 : 2 proportion. It should be noted, however, that these faults are not embedded in long cubic or hexagonal sequences: pure cubic or hexagonal sequences with more than three layers are rare in the nanoconfined ice.

Table 1 Percentages of liquid and cubic, hexagonal and interstitial ice in the crystallized nanopores. 1st and 1st + 2nd shells denote the layers of water within 0.35 and 0.55 nm of the pore surface, respectively

	%Hexagonal (H)	%Cubic (C)	%Interfacial (I)	%Liquid (L)
All water, 195 K	11.2 ± 3.3	23.2 ± 3.6	28.2 ± 1.0	37.4 ± 4.4
1st shell, 195 K	2.2 ± 1.1	4.0 ± 1.9	22.5 ± 3.4	71.3 ± 3.1
All water, 220 K	7.9 ± 2.5	19.2 ± 2.2	22.3 ± 1.9	50.6 ± 2.1
1st shell, 220 K	0.8 ± 0.4	2.5 ± 0.8	12.8 ± 1.7	83.9 ± 3.8
1st + 2nd shell, 220 K	1.7 ± 0.5	4.4 ± 0.9	17.1 ± 1.8	76.8 ± 4.1

D Melting point of ice in the nanopore

In the simulations, we observed melting of ice in the nanopore at 225 K but not at 220 K. We assign the melting point of ice in the pore to $T_m^{pore} = 222.5 \pm 2.5$ K. This is in excellent agreement with the $215 \leq T_m^{pore} \leq 231$ K predicted for $R = 1.5$ nm by the Gibbs–Thomson equation with the K_{GT} and d fitted from experiments in MCM-41 and SBA-15 pores.[5–7] The agreement with the experiments confirms that the depression in the melting point is determined by the properties of pure water and ice (well reproduced by the mW model), and not the details of the water–pore interaction.[11] It is not possible to determine K_{GT} and d from a single pore radius. Nevertheless, we note that the amount of water in the pore, about one monolayer ($d \sim 0.35$ nm) at $T_f^{pore} = 195$ K, increased to about two monolayers at 220 K. Table 1 shows that the total fraction of liquid in the pore increased from 37% at 195 K to 51% at 220 K, and that the fraction of liquid in the water layer that contacts the pore wall increased from 71.3% at 195 K to 83.9% at 220 K. Moreover, at 220 K the liquid makes up $\frac{3}{4}$ of the total water in the first plus second layer combined, $d < 0.55$ nm from the surface of the pore. The width of the liquid layer observed in the simulation just below T_m^{pore} is ~0.5 nm, in good agreement with the 0.35–0.6 nm obtained from the fit of the experimental T_m^{pore} to the modified Gibbs–Thomson equation.[5–7] The observed increase in the amount of liquid in equilibrium with the pore as the temperature approaches the melting point confirms the conjecture of Liu *et al.*[13] of an interfacial region where water reversibly converts to a disordered form of ice (that we call interfacial ice) at lower temperatures. Premelting has been observed for other liquids confined by cylindrical nanopores and simple models predict a continuous increase of the liquid layer on heating followed by a sharp transition at T_m^{pore}.[53]

The enthalpy of melting of water in the nanopore was 42% of the bulk value. A comparable reduction in the value of the enthalpy of fusion has been reported in experimental studies.[6,8] The ratio $\Delta H_m^{pore}/\Delta H_m^{bulk}$ observed in this work agrees quantitatively with that of ref. 8 for a 3 nm diameter MCM-41 pore, but it is larger than that reported in ref. 6 for the same diameter pore. It should be noted that these two works differ in the assignment of the size of the pore: while $R = 1.5$ nm could correspond to MCM-41 C12 according to ref. 6, that diameter would be intermediate between those of MCM-41 C14 and MCM-41 C16 according to ref. 8. The reduction in the enthalpy of melting we observe is consistent with the lower fraction of ice in the pore, about 50% of the total amount of confined water.

5. Conclusions

In this work, molecular simulations were used to determine the existence and location of liquid water in crystallized nanopores, the structure of the nanoconfined ice, and the microscopic mechanism of nucleation and growth of ice in the pores. To the best of our knowledge, this is the first simulation study that reports the nucleation and structure of ice in hydrophilic nanopores. The main challenges to this endeavor have been the difficulty in nucleating ice in simulations and a lack of a simple rotationally invariant methods to identify ice and its polymorphs. In this work, we surmounted the first through the use of an accurate and efficient coarse-grained model of water and the second through the development of a simple method to classify each molecule as belonging to liquid, hexagonal, cubic or interfacial ice based on the number of staggered and eclipsed water–water intermolecular bonds with its four closest neighbors.

The equilibrium melting temperature of the confined ice in the 3 nm pore with water walls is in excellent agreement with the experimental melting point in MCM-41 silica with the same pore diameter. This may either indicate that the interactions of water with a water wall and with a silica wall are similar, or that the ice–liquid equilibrium temperature is not very sensitive to the details of the water–pore interaction. The latter possibility is supported by the results of Findenegg and coworkers on surface modified SBA-15.[11] Determination of the melting temperature for other water–pore potentials is necessary to clarify the weights of the two arguments.

The simulations confirm conjectures on the existence of a liquid layer at the surface of the pore and its widening as the temperature approaches the melting point.[13] At 220 K, about 3 K below the melting point, the liquid encompasses two water layers, while at 195 K, the freezing temperature, the liquid extends over one monolayer. The water–water and water–wall interactions are identical in this study, thus the formation of a premelted layer does not arise from a difference in interactions but from the fact that the liquid can accommodate better to the structure of the wall than the crystal. For surfaces that present strong water absorption, known to be the case in titania nanopores,[54] the wall will be paved with an additional adsorbed water layer—thus essentially making it a narrower pore with a water surface, as the one considered in this study. The situation may be different for partially wetting and non-wetting interfaces, for which the formation of a liquid layer at the pore surface may not offer a free energy advantage.

The nucleation of ice in the pore is homogeneous: the pore wall surface does not assist in the formation of the ice

crystallites; it does not even wet the nuclei. From the analysis of the largest ice nucleus *vs.* time in the isothermal crystallization trajectories and the quenching runs, we estimate that the critical nucleus contains $\sim$75 to 100 molecules and its radius of gyration is $\sim$1.0 nm, close to the 1.5 nm radius of the pore, thus hindering nucleation. The effect should be more pronounced for narrower pores, for which crystallization is not observed in the experiments.[6,11] Stacking layers become apparent in nuclei of $\sim$150 molecules, and their orientation is maintained when these crystallites grow, giving rise to varied assortments of crystal orientations with respect to the axis of the pore. The nanoconfined ice is rich in stacking faults, in agreement with the interpretation of X-ray diffraction of Morishige and Uematsu,[20] and neutron diffraction of Dore and coworkers.[13–15] We find a 2 : 1 ratio of cubic to hexagonal layers in the confined ice. This is the same ratio derived from the neutron diffraction spectra of ice I recovered by decompression of ice V.[17] A difference, however, is the abundance of both growth and deformation faults in the confined ice, while the former are absent in the bulk ice. In spite of the relative abundance of cubic layers, the confined ice should not be considered a cubic ice with defects: *Ic* (and *Ih*) domains with more than three layers are rare in this narrow pore.

The results and insights from NMR, DSC, neutron and X-ray diffraction experiments and simulations are complementary and yield a more complete picture of the state of water in nanoporous materials. This work shows the suitability of coarse-grained simulations with the mW model in describing the phase behavior and structure of water in crystallized nanopores. The very good agreement between the simulations of water confined in a pore with water walls and the experiments reported for water in nanoporous silica suggests that either the details of the wall–water interaction potential have small effect on the ice-structure and liquid–ice equilibrium in nanopores or that the interactions of water with a silica wall and a water wall are similar. These are both interesting possibilities that we will investigate in the future.

Acknowledgements

This work was supported by the Beckman Young Investigator Program (V.M.) and a collaborative research grant of the Agencia Nacional de Promoción Científica y Tecnológica de Argentina (V.M. and D.S.) K.W. acknowledges a student fellowship from DAAD and the exchange program at TU-Braunschweig for supporting his stay at the University of Utah. We thank the Center of High Performance Computing of the University of Utah for allocation of computing time.

References

1 C. Alba-Simionesco, B. Coasne, G. Dosseh, G. Dudziak, K. E. Gubbins, R. Radhakrishnan and M. Sliwinska-Bartkowiak, *J. Phys.: Condens. Matter*, 2006, **18**, R15.
2 I. Brovchenko and A. Oleinikova, *Interfacial and Confined Water*, Elsevier, Amsterdam, 2008.
3 I. Shenderovich, G. Buntkowsky, A. Schreiber, E. Gedat, S. Sharif, J. Albrecht, N. Golubev, G. Findenegg and H. Limbach, *J. Phys. Chem. B*, 2003, **107**, 11924.
4 I. G. Shenderovich, D. Mauder, D. Akcakayiran, G. Buntkowsky, H.-H. Limbach and G. H. Findenegg, *J. Phys. Chem. B*, 2007, **111**, 12088.
5 R. Schmidt, E. Hansen, M. Stöcker, D. Akporiaye and O. Ellestad, *J. Am. Chem. Soc.*, 1995, **117**, 4049.
6 S. Jahnert, F. V. Chavez, G. E. Schaumann, A. Schreiber, M. Schonhoff and G. H. Findenegg, *Phys. Chem. Chem. Phys.*, 2008, **10**, 6039.
7 A. Schreiber, I. Ketelsen and G. H. Findenegg, *Phys. Chem. Chem. Phys.*, 2001, **3**, 1185.
8 S. Kittaka, S. Ishimaru, M. Kuranishi, T. Matsuda and T. Yamaguchi, *Phys. Chem. Chem. Phys.*, 2006, **8**, 3223.
9 K. Morishige and K. Kawano, *J. Chem. Phys.*, 1999, **110**, 4867.
10 K. Morishige, H. Uematsu and N. Tateishi, *J. Phys. Chem. B*, 2004, **108**, 7241.
11 G. H. Findenegg, S. Jaehnert, D. Akcakayiran and A. Schreiber, *ChemPhysChem*, 2008, **9**, 2651.
12 J. B. W. Webber, J. C. Dore, J. H. Strange, R. Anderson and B. Tohidi, *J. Phys.: Condens. Matter*, 2007, **19**, 415117.
13 E. Liu, J. C. Dore, J. B. W. Webber, D. Khushalani, S. Jähnert, G. H. Findenegg and T. Hansen, *J. Phys.: Condens. Matter*, 2006, **18**, 10009.
14 J. Seyed-Yazdi, H. Farman, J. C. Dore, J. B. W. Webber and G. H. Findenegg, *J. Phys.: Condens. Matter*, 2008, **20**, 205108.
15 J. Seyed-Yazdi, H. Farman, J. C. Dore, J. B. W. Webber, G. H. Findenegg and T. Hansen, *J. Phys.: Condens. Matter*, 2008, **20**, 205107.
16 W. F. Kuhs, D. V. Bliss and J. L. Finney, *J. Phys. Colloques*, 1987, **48**, 631.
17 T. C. Hansen, M. M. Koza and W. F. Kuhs, *J. Phys.: Condens. Matter*, 2008, **20**, 285104.
18 T. C. Hansen, A. Falenty and W. F. Kuhs, "Modelling ice *Ic* of different origin and stacking faulted hexagonal ice using neutron powder diffraction data", in *Physics and Chemistry of Ice*, ed. W. F. Kuhs, RSC Publishing, Royal Society of Chemistry, Cambridge, 2006, p. 201.
19 T. C. Hansen, M. M. Koza, P. Lindner and W. F. Kuhs, *J. Phys.: Condens. Matter*, 2008, **20**, 285105.
20 K. Morishige and H. Uematsu, *J. Chem. Phys.*, 2005, **122**, 044711.
21 M. Matsumoto, S. Saito and I. Ohmine, *Nature*, 2002, **416**, 409.
22 L. Vrbka and P. Jungwirth, *J. Phys. Chem. B*, 2006, **110**, 18126.
23 K. Koga and H. Tanaka, *J. Chem. Phys.*, 2005, **122**, 104711.
24 K. Koga, H. Tanaka and X. C. Zeng, *Nature*, 2000, **408**, 564.
25 K. Koga, X. C. Zeng and H. Tanaka, *Phys. Rev. Lett.*, 1997, **79**, 5262.
26 P. Kumar, F. W. Starr, S. V. Buldyrev and H. E. Stanley, *Phys. Rev. E: Stat., Nonlinear, Soft Matter Phys.*, 2007, **75**, 011202.
27 N. Giovambattista, P. J. Rossky and P. G. Debenedetti, *Phys. Rev. Lett.*, 2009, **102**, 050603.
28 N. Giovambattista, P. J. Rossky and P. G. Debenedetti, *Phys. Rev. E: Stat., Nonlinear, Soft Matter Phys.*, 2006, **73**, 041604.
29 R. Zangi and A. E. Mark, *J. Chem. Phys.*, 2003, **119**, 1694.
30 R. Zangi, *J. Phys.: Condens. Matter*, 2004, **16**, S5371.
31 K. Koga, G. T. Gao, H. Tanaka and X. C. Zeng, *Nature*, 2001, **412**, 802.
32 R. Radhakrishnan and B. L. Trout, *J. Am. Chem. Soc.*, 2003, **125**, 7743.
33 A. V. Brukhno, J. Anwar, R. Davidchack and R. Handel, *J. Phys.: Condens. Matter*, 2008, **20**, 494243.
34 D. Quigley and P. M. Rodger, *J. Chem. Phys.*, 2008, **128**, 154518.
35 H. Tanaka and I. Okabe, *Chem. Phys. Lett.*, 1996, **259**, 593.
36 R. G. Fernandez, J. L. F. Abascal and C. Vega, *J. Chem. Phys.*, 2006, **124**, 144506.
37 C. Vega, E. Sanz and J. L. F. Abascal, *J. Chem. Phys.*, 2005, **122**, 114507.
38 C. Vega, J. L. F. Abascal, E. Sanz, L. G. MacDowell and C. McBride, *J. Phys.: Condens. Matter*, 2005, **17**, S3283.
39 J. L. F. Abascal, E. Sanz, R. G. Fernandez and C. Vega, *J. Chem. Phys.*, 2005, **122**, 234511.
40 V. Molinero and E. B. Moore, *J. Phys. Chem. B*, 2009, **113**, 4008.
41 E. B. Moore and V. Molinero, *J. Chem. Phys.*, 2009, **130**, 244505.
42 L. C. Jacobson, W. Hujo and V. Molinero, *J. Phys. Chem. B*, 2009, **113**, 10298.
43 W. Zhang, C. He, J. Lian and Q. Jiang, *Chem. Phys. Lett.*, 2006, **421**, 251.

44 P. J. Steinhardt, D. R. Nelson and M. Ronchetti, *Phys. Rev. Lett.*, 1981, **47**, 1297.
45 P. R. Ten Wolde, M. J. Ruiz-Montero and D. Frenkel, *J. Chem. Phys.*, 1996, **104**, 9933–9947.
46 S. J. Plimpton, *J. Comput. Phys.*, 1995, **117**, 1.
47 J. R. Errington and P. G. Debenedetti, *Nature*, 2001, **409**, 318.
48 L. S. Ramsdell, *Am. Mineral.*, 1947, **32**, 64.
49 C. A. Angell, *Annu. Rev. Phys. Chem.*, 2004, **55**, 559.
50 P. G. Debenedetti, *J. Phys.: Condens. Matter*, 2003, **15**, R1669.
51 E. B. Moore and V. Molinero, Liquid–liquid transformation in water controls the temperature of homogeneous nucleation of ice, manuscript in preparation.
52 O. Yamamuro, M. Oguni, T. Matsuo and H. Suga, *J. Phys. Chem. Solids*, 1987, **48**, 935–942.
53 D. Wallacher and K. Knorr, *Phys. Rev. B: Condens. Matter Mater. Phys.*, 2001, **63**, 104202.
54 E. Mamontov, D. J. Wesolowski, L. Vlcek, P. T. Cummings, J. Rosenqvist, W. Wang and D. R. Cole, *J. Phys. Chem. C*, 2008, **112**, 12334.

